

# InstantSfM: Towards GPU-Native SfM for the Deep Learning Era

Jiankun Zhong<sup>\*1,3</sup>, Zitong Zhan<sup>\*2</sup>, Quankai Gao<sup>\*1</sup>, Ziyu Chen<sup>1</sup>, Haozhe Lou<sup>1</sup>,  
Jiageng Mao<sup>1</sup>, Ulrich Neumann<sup>1</sup>, Chen Wang<sup>2</sup>, and Yue Wang<sup>1</sup>

<sup>1</sup>University of Southern California

<sup>2</sup>University at Buffalo

<sup>3</sup>Tsinghua University

**Abstract**—Structure-from-Motion (SfM) is a fundamental technique for recovering camera poses and scene structure from multi-view imagery, serving as a critical upstream component for applications ranging from 3D reconstruction to modern neural scene representations such as 3D Gaussian Splatting. However, most mature SfM systems remain CPU-centric and built upon traditional optimization toolchains, creating a growing mismatch with modern GPU-based, learning-driven pipelines and limiting scalability in large-scale scenes. While recent advances in GPU-accelerated bundle adjustment (BA) have demonstrated the potential of parallel sparse optimization, extending these techniques to build a complete global SfM system remains challenging due to unresolved issues in metric scale recovery and numerical robustness. In this paper, we implement a fully GPU-based and PyTorch-compatible global SfM system, named InstantSfM, to integrate seamlessly with modern learning pipelines. InstantSfM embeds metric depth priors directly into both global positioning and BA through a depth-constrained Jacobian structure, thereby resolving scale ambiguity within the optimization framework. To ensure numerical stability, we employ explicit filtering of under-constrained variables for the Jacobian matrix in an optimized GPU-friendly manner. Extensive experiments on diverse datasets demonstrate that InstantSfM achieves state-of-the-art efficiency while maintaining reconstruction accuracy comparable to both established classical pipelines and recent learning-based methods, showing up to  $\sim 40\times$  speedup over COLMAP on large-scale scenes.<sup>1</sup>

## I. INTRODUCTION

Structure-from-Motion (SfM) is a foundational technique in computer vision and robotics that jointly estimates camera poses and reconstructs 3D structure from multi-view imagery [1], [2]. It supports a wide range of applications including cultural heritage digitization [3], autonomous driving [4], and dynamic scene understanding [5], [6]. SfM also serves as a critical component for downstream 3D vision pipelines, such as multi-view stereo (MVS) dense reconstruction [7] and neural scene representations, such as neural radiance fields (NeRF) [8] and 3D Gaussian Splatting (3DGS) [9].

Despite its importance, most existing SfM systems [10], [11] remain largely CPU-based and are implemented in C++-based optimization toolchains [12]. Their architectures reflect design principles established prior to the widespread adoption of GPU-native deep learning frameworks, which makes seamless integration with modern data-driven pipelines challenging. In contrast, learning-based SfM front-ends [5],

[13] and neural rendering approaches [14] are built around parallel GPU computation and tightly coupled with PyTorch. This architectural gap reduces the practicality of SfM in modern vision pipelines: it is often treated as an offline processing stage outside PyTorch and can require hours to days to process large-scale image collections [11]. More broadly, recent robotics research has begun exploring tighter integration between learned models and optimization-based decision modules within a unified frameworks [15], [16].

This gap has motivated growing interest in GPU-based bundle adjustment (BA) [17], an important component of SfM for refining camera poses and 3D scene structure into a globally consistent reconstruction. BA simultaneously optimizes the 3D point positions and camera parameters by minimizing the reprojection errors. Recent studies demonstrate that large-scale BA can be efficiently accelerated on GPUs using PyTorch-native sparse data structures and GPU-parallelized operators to enable Levenberg-Marquardt (LM) optimization within a user-friendly interface, enabling execution in eager mode [17]. However, extending such GPU-accelerated BA into a complete, global SfM system introduces several fundamental challenges that remain largely unresolved. Additionally, implementing the entire system in PyTorch programming primitives for an optimal usability poses further challenges in balancing performance and maintainability.

First, existing GPU-based BA frameworks [18], [19], [20] are largely specialized for optimizing camera reprojection loss and offer limited support for incorporating additional geometric constraints; Therefore, global SfM pipelines built upon them inherit this restricted residual formulation and are difficult to extend beyond reprojection-based objectives. In addition, robotics applications typically require metric consistency and the fusion of additional sensing modalities, such as depth measurements from RGB-D sensors and learned depth models. Incorporating these depth constraints into global SfM optimization requires redefining residuals and restructuring Jacobian construction to accommodate heterogeneous, partially invalid depth maps and irregular sparsity patterns. These challenges are not well supported by existing GPU-based optimization frameworks, which lack the flexibility needed for robotics integration.

Second, common outliers in feature detection and matching can severely compromise numerical robustness and optimization stability of SfM. While robust loss functions in BA can

<sup>\*</sup>These authors contributed equally to this work.

<sup>1</sup>Code available at [github.com/cre185/InstantSfM](https://github.com/cre185/InstantSfM)

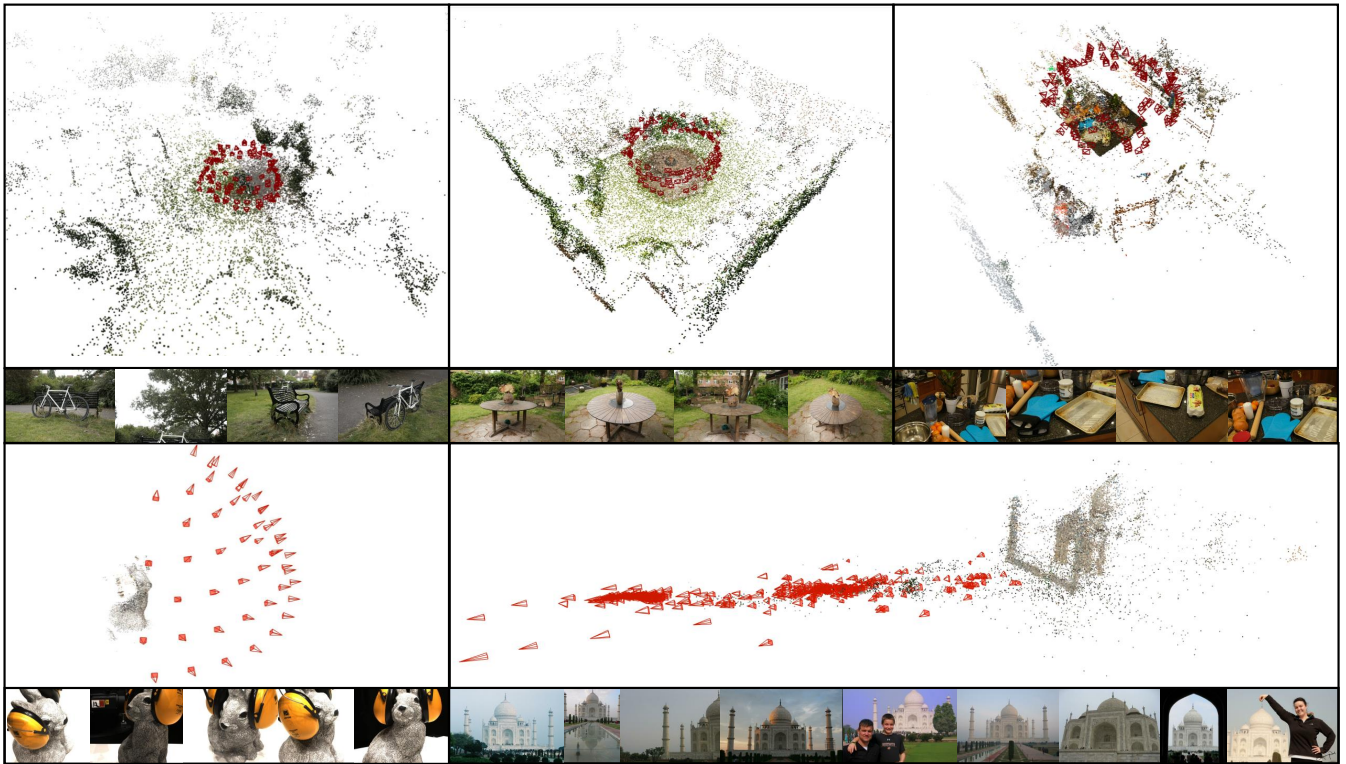


Fig. 1. Qualitative results on various datasets. Camera frustums as red are visualized for illustrating the estimated camera poses. Input images for each scene are sampled below each reconstruction.

alleviate the influence of such outliers, they are insufficient for global SfM, where a single unstable optimization step can propagate errors and corrupt the entire reconstruction. However, aggressive outlier filtering or highly uneven outlier distributions can leave cameras or 3D points under-constrained, resulting in rank-deficient normal equations in the LM solver and potential optimization failure.

Motivated by these challenges, we present InstantSfM, a PyTorch-compatible global SfM system allowing seamless integration with modern data-driven learning pipelines on GPU. Our approach builds upon recent advances in GPU-accelerated sparse BA [17] and extends them into a complete SfM framework addressing the aforementioned limitations.

Specifically, InstantSfM introduces two key technical contributions. First, we introduce a depth-constrained Jacobian structure that enables metric depth priors obtained from depth sensors or monocular depth estimators to be directly embedded into global positioning and BA. This formulation resolves the inherent scale ambiguity of SfM within the optimization process, allowing camera poses and 3D points to be recovered at a consistent metric scale. Second, we focus on ensuring numerical robustness in large-scale GPU-based global optimization. To address the under-constrained variable problem arising from outlier filtering, our system explicitly monitors variable observability and removes under-constrained elements prior to optimization in a highly efficient SIMD GPU programming model [17], preserving the positive definiteness and full rank of the normal equations and preventing common solver failures in global SfM.

Together, these contributions yield a scalable and robust

global SfM system that aligns with modern GPU-based workflows. InstantSfM achieves state-of-the-art efficiency, delivering  $1.5\times$  to  $40\times$  speedup over COLMAP and up to  $12\times$  over GLOMAP across scenes ranging from 100 to 5000 images, while maintaining accuracy comparable to both classical SfM pipelines and recent learning-based methods. InstantSfM is the first global SfM based on PyTorch, enabling seamless integration with existing vision and learning frameworks, and making large-scale, metric-consistent SfM more accessible to a broad range of research communities.

## II. RELATED WORKS

**Correspondence Search.** SfM typically begins with feature detection on a given image set, denoted as  $\mathcal{I} = \{I_1, \dots, I_n\}$ , and extracts either sparse [21], [22] or dense [23], [24] feature descriptors  $\mathcal{F} = \{f_1, \dots, f_n\}$  to establish view correspondences. The feature detections are then matched by calculating the feature affinities or more advanced matching algorithms [25]. Based on these matching results, homography  $\mathbf{H}$  and fundamental matrix  $\mathbf{F}$  are estimated to model pairwise view transformations. Since outliers are inevitably involved in feature extraction, robust estimation algorithms such as RANSAC [26] can greatly improve the accuracy of correspondence search.

**Reconstruction.** Given the estimated scene graph from the correspondence search, reconstruction aims to recover the intrinsic and extrinsic camera parameters, along with the scene structure represented as a set of 3D points triangulated from 2D features [27]. For estimating camera parameters, one prevalent option is incremental reconstruction [10], [1], [28], which

progressively integrates pairwise view transformations into the existing 3D map reconstruction. Incremental approaches are well-known to be robust against outliers as it iteratively filters outlier and refines pose, but they also suffer from drift and low computational efficiency [29]. Global approaches [11], [30], [31], [32] estimate all 3D points and camera poses at once. They employ strategies such as rotation averaging and global positioning, which provide an initial guess of camera poses for BA. Although global SfM approaches may lack per-step outlier filtering or rejection, various designs have been proposed to mitigate drift and error. These methods incorporate 3D cues such as reference planes, line segments, and vanishing points or employ re-triangulation to enhance the robustness of BA [11].

**Learning-Based SfM.** Significant progress has been made in learning-based SfM, including end-to-end differentiable SfM pipelines such as VGGsFm [33]. An orthogonal line of research [34], [13] approaches the same goal in a feed-forward manner by leveraging pretrained image-3D encoder such as DUS3R [35]. However, these methods are either computationally expensive in terms of time and memory, limited to small or moderate-scale scenes, or lack guarantees for generalization to out-of-distribution cases.

**Non-Linear Optimization.** BA is a key optimization method used to refine camera parameters and 3D scene structure by minimizing the reprojection error. It boils down to solving a non-linear least squares problems, whose size scales with the number of images and 3D points. Since there is no general closed-form solution, most of the literature focuses on developing efficient second-order numerical solvers for BA, ranging from Gauss-Newton methods to the more robust Levenberg-Marquardt (LM) algorithm [36]. Widely-used BA frameworks are either C++-based, enabling parallelization on CPU such as Ceres [12] and GTSAM [37], or PyTorch implementations such as DeepLM [19], which utilize PyTorch’s autograd engine for Jacobian calculations.

**GPU-based BA.** Recent work has explored GPU-based BA optimizations [17], demonstrating significant acceleration through sparse matrix operations and cuSPARSE implementations. Building upon these sparse-aware techniques, we extend the approach to encompass both BA and global positioning within a unified PyTorch framework. Although existing tools achieve high accuracy, they either remain inefficient for large-scale BA problems [12] or cannot generalize to more types of problems [19]. An orthogonal line of research, such as [38], proposes a convex relaxation of the original BA objective, however not designed to handle outliers.

### III. BACKGROUND OF GLOBAL SFM

Our contributions center on extending sparsity-aware non-linear least squares optimization to support metric depth constraints and robust outlier handling within a unified GPU framework. We introduce the formulations of GP and BA and analyze the sparse structure of their Jacobians, which directly motivates our technical designs in Sec. IV.

#### A. Global Camera Pose Estimation

Global camera pose estimation plays an important role in initializing camera extrinsics before iterative BA. It consists of rotation averaging [39] and translation averaging [40], [30]. It is worth mentioning that GLOMAP [11] proposes GP as a more robust alternative to translation averaging by jointly estimating locations of camera centers and 3D points with fixed camera rotations. Denote the number of cameras and points by  $C$  and  $P$ , respectively. The optimization objective can be formulated as follows:

$$\theta = \arg \min_{\mathbf{X}, \mathbf{t}, s} \sum_{i=1}^C \sum_{j=1}^P \rho(\| \underbrace{\mathbf{v}_{ij} - s_{ij}(\mathbf{X}_j - \mathbf{t}_i)}_{\mathbf{u}_{ij}} \|_2^2), \quad (1)$$

where optimizable parameters  $\theta$  include 3D point locations  $\mathbf{X} \in \mathbb{R}^{P \times 3}$ , camera centers  $\mathbf{t} \in \mathbb{R}^{C \times 3}$  and scalar scales  $s_{ij}$  for every valid observation;  $\rho$  is Huber [41] robustifier and  $\mathbf{v}$  denotes pixel ray direction vectors from camera centers to 2D feature points. After convergence, each triangulated 3D point  $\mathbf{X}_k$  should lie in its corresponding pixel ray emitted from visible cameras ensuring global consistency. The per-observation scale variables  $s_{ij}$  in this formulation serve as the entry point for our depth-constrained extension in Sec. IV.

#### B. Bundle Adjustment

Global camera pose estimation estimates camera rotations, camera centers, and 3D points independently with limited accuracy. BA can further refine the above estimations together with camera intrinsics. Similar to GP, BA is formulated as the least squares problem, minimizing the reprojection errors  $\mathbf{r} \in \mathbb{R}^{2 \times CP}$  of 3D points across visible camera views:

$$\theta = \arg \min_{\mathbf{X}, \zeta, \mathbf{K}} \sum_{i=1}^C \sum_{j=1}^P \rho(\| \underbrace{\Pi(\zeta_i, \mathbf{X}_j, \mathbf{K}_i) - \mathbf{x}_{ij}}_{\mathbf{r}_{ij}} \|_2^2), \quad (2)$$

where optimizable parameters  $\theta$  include camera intrinsics  $\mathbf{K} \in \mathbb{R}^{C \times 1}$  and extrinsics  $\zeta = \{\mathbf{t}, \mathbf{o}\} \in \mathbb{R}^{C \times 7}$  consisting of camera centers  $\mathbf{t} \in \mathbb{R}^{C \times 3}$  and quaternions  $\mathbf{o}_i \in \mathbb{SO}(3)$ .  $\mathbf{r}_{ij}$  denotes the reprojection error between a 2D feature point  $\mathbf{x}_{ij}$  on the  $i$ -th camera and the  $j$ -th 3D point  $\mathbf{X}_j$  projected to the same camera. We extend this formulation with metric depth residuals and robust outlier handling in Sec. IV.

#### C. Levenberg-Marquardt Algorithm

We use the LM algorithm for both the GP and BA objectives. It solves the following linear system for an update step  $\Delta\theta$  at each iteration,

$$(\mathbf{J}^\top \mathbf{J} + \lambda \text{diag}(\mathbf{J}^\top \mathbf{J})) \Delta\theta = -\mathbf{J}^\top \mathbf{r}, \quad (3)$$

where  $\mathbf{J} = \frac{\partial \mathbf{r}}{\partial \theta}$  is the Jacobian matrix. For BA,  $\mathbf{J} \in \mathbb{R}^{2CP \times (7C+3P)}$ , which is infeasible to store densely in GPU memory even at moderate scale. Since the scale of  $\mathbf{J}$  directly determines runtime, we build upon sparse-aware BA techniques [17] and extend the sparse data structure to encompass global positioning within a unified framework.

#### IV. METHODOLOGY

InstantSfM introduces two core technical contributions. First, we propose a *depth-constrained Jacobian structure* (Sec. IV-A) that embeds metric depth priors as live constraints directly inside the GP and BA optimization, allowing scale to propagate directly to unconstrained cameras and points through the shared sparse structure. Second, to ensure numerical robustness under inevitable outlier contamination, we introduce *dynamic parameter extraction* (Sec. IV-B), which identifies and removes outliers on-the-fly in each LM iteration and maintains a full-rank parameter space throughout optimization, a capability not supported by existing CPU- and GPU-based solvers that assume a static residual structure.

##### A. Depth-Constrained Jacobian Structure

SfM is scale-ambiguous: camera poses and 3D structure can only be recovered up to an unknown global scale factor from image observations alone. Classical pipelines such as COLMAP have no mechanism to incorporate metric depth available from RGB-D sensors or monocular depth estimators into the reconstruction process itself; depth can only be applied in post-processing to rigidly align the finished reconstruction to a known scale. This fitting is incapable of correcting accumulated drift or resolving local scale inconsistencies that arise during reconstruction, nor does it offer any benefit in estimating the camera poses and 3D structure, leaving the metric depth priors largely unexploited. However, recovering reconstructions at consistent metric scale is important for robotics applications such as physics-based simulation [6] and cross-modal depth fusion [42], where absolute distances must be preserved. To fulfill this need, our pipeline instead embeds metric depth priors as joint residual constraints directly inside both the GP and BA optimization stages, allowing depth prior to facilitate reconstruction through the shared sparse Jacobian structure. We first introduce the formulation of depth-constrained optimization and then describe how we implement it in a GPU-friendly manner within the LM optimizer.

**GP.** The GP objective (1) contains a per-observation scale variable  $s_{ij}$ , which represents the inverse depth of point  $\mathbf{X}_j$  as seen from camera  $i$ : since  $\mathbf{v}_{ij}$  is a unit-normalized ray direction,  $s_{ij}$  scales the ray to reach  $\mathbf{X}_j$ . When a metric depth measurement  $\hat{d}_{ij}$  is available from the depth map of camera  $i$ , we fix this otherwise free variable to its known value  $s_{ij} = 1/\hat{d}_{ij}$ , removing it from the set of optimized parameters. Substituting into (1), the depth-constrained residual becomes:

$$\mathbf{u}_{ij} = \mathbf{v}_{ij} - \frac{\mathbf{X}_j - \mathbf{t}_i}{\hat{d}_{ij}}, \quad (4)$$

and the GP objective for points with valid depth measure:

$$\theta = \arg \min_{\mathbf{X}, \mathbf{t}} \sum_{i=1}^C \sum_{j=1}^P \rho(\|\mathbf{v}_{ij} - \frac{\mathbf{X}_j - \mathbf{t}_i}{\hat{d}_{ij}}\|_2^2). \quad (5)$$

**BA.** To incorporate metric depth into the BA stage, we introduce an additional depth residual term following [43]:

$$\mathbf{r}_{ij}^d = \frac{1}{\text{Depth}(\zeta_i, \mathbf{X}_j, \mathbf{K}_i)} - \frac{1}{\hat{d}_{ij}}, \quad (6)$$

where  $\text{Depth}(\zeta_i, \mathbf{X}_j, \mathbf{K}_i)$  is the depth calculated from estimated cameras and points, and the whole BA formulation:

$$\theta = \arg \min_{\mathbf{X}, \zeta, \mathbf{K}} \sum_{i=1}^C \sum_{j=1}^P \rho(\mathbf{r}_{ij} + \lambda_d \mathbf{r}_{ij}^d), \quad (7)$$

where  $\lambda_d$  is the weighting parameter for the depth constraint. A key challenge when incorporating monocular depth priors is that depth map is inherently incomplete: regions such as sky, specular surfaces, or distant clutter produce invalid estimates. Naively masking these points would remove useful reprojection constraints and destabilize the sparse normal equations. We address this through a *heterogeneous depth-masking* scheme operated directly on the sparse Jacobian.

**In GP,** the primary role is to provide a metric-scale initialization for 3D point positions. Points with valid depth measurements serve as metric anchors: since their scale  $s_{ij}$  is already fixed by the known depth ( $s_{ij} = 1/\hat{d}_{ij}$ ), they are algebraically *pinned* by removing their  $s_{ij}$  variables from the Jacobian. These anchored points then propagate metric scale constraints through shared camera centers to points lacking valid depth, which remain as free parameters optimized normally. This selective treatment requires specialized sparse block assembly routines that dynamically partition all point observations into constrained and unconstrained subsets, a design not yet considered by existing GPU BA frameworks.

Traditional CPU-based solvers would handle this by checking validity of each observation sequentially and adding them to the sparse Jacobian dictionary [17] one-by-one, but this approach is inefficient on GPU due to thread divergence and irregular memory access patterns. Instead, our goal is to design a unified Jacobian structure that can be constructed in a single pass, while still effectively removing the influence of invalid depth measurements on the optimization.

To handle invalid depth entries, we introduce a binary mask  $m_{ij}$  indicating the validity of each depth measurement, where  $m_{ij} = 1$  if  $\hat{d}_{ij}$  is valid and 0 otherwise. This flag partitions the full scale parameter set into pinned and free subsets:

$$\mathcal{S}_{\text{pin}} = \{(i, j) \mid m_{ij} = 1\}; \mathcal{S}_{\text{free}} = \{(i, j) \mid m_{ij} = 0\}. \quad (8)$$

Only  $\mathcal{S}_{\text{free}}$  contributes columns to the Jacobian  $\mathbf{J}$  entering the normal equations; columns of  $\mathcal{S}_{\text{pin}}$  are structurally excluded before the LM solve. This column-level exclusion is computed via a parallel set-membership test on GPU that identifies the free-scale indices and compacts the Jacobian accordingly.

Although the pinned scales are removed as optimization variables, their metric information is not lost. It is implicitly transferred to the rest of the scene through the *shared camera-center columns* of  $\mathbf{J}$ . Specifically, from the GP residual  $\mathbf{u}_{ij} = \mathbf{v}_{ij} - s_{ij}(\mathbf{X}_j - \mathbf{t}_i)$ , the Jacobian block with respect to the camera center is  $\partial \mathbf{u}_{ij} / \partial \mathbf{t}_i = s_{ij} \mathbf{I}$ , so every observation from the same camera  $i$  contributes to the same camera-center block-column of  $\mathbf{J}$ . In the normal equations  $\mathbf{J}^\top \mathbf{J}$ , this yields a non-zero off-diagonal coupling between any free scale  $s_{i'j'} \in \mathcal{S}_{\text{free}}$  and the camera center  $\mathbf{t}_i$  shared with pinned observations. The pinned observations impose metrically-scaled gradients on  $\mathbf{t}_i$  (since their  $s_{ij} = 1/\hat{d}_{ij}$  encodes the

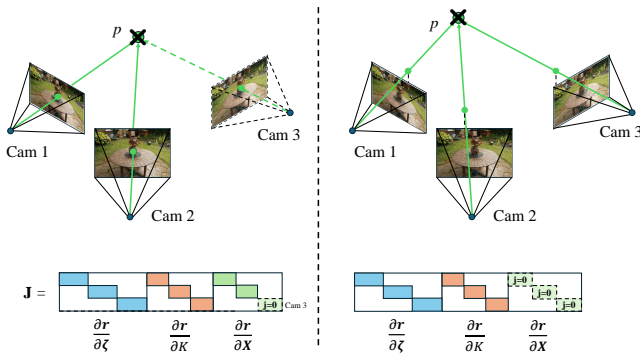


Fig. 2. We illustrate the motivation behind our robust outlier removal. Outliers often arise from noisy feature extraction or incorrect feature matching and are typically filtered based on their visibility across multiple cameras. A 3D point is treated as an outlier and removed if it is observed by fewer cameras than a predefined threshold (3 in the figure above) or if none of its reprojections fall within any camera frustum. However, this “removal” can lead to numerical issues during optimization (see Sec. IV-B).

known metric depth), and through this coupling the updated  $\mathbf{t}_i$  in turn drives the free-scale update, propagating metric consistency across the entire scene.

**In BA**, we preserve invalid-depth points in the Jacobian but assign their inverse depth  $\frac{1}{d_{ij}}$  a small sentinel value. This is because points without valid depths are often misaligned points or correspond to points far away. This suppresses the depth residuals but preserves reprojection constraints. The unified formulation gracefully handles partial depth coverage without sacrificing sparse matrix conditioning or introducing additional outlier-rejection heuristics.

To implement this efficiently on GPU, we use the same validity mask  $m_{ij}$  to modulate the depth residuals during Jacobian construction. Specifically, invalid-depth entries are handled by defining the effective inverse-depth reference uniformly for all observations as:

$$\tilde{d}_{ij}^{-1} = m_{ij} \cdot \hat{d}_{ij}^{-1}, \quad (9)$$

so the depth residual  $\mathbf{r}_{ij}^d = 1/\text{Depth}(\cdot) - \tilde{d}_{ij}^{-1}$  collapses to a reprojection-only term for invalid points. Because the formula is structurally identical regardless of validity, the residual tensor is evaluated in one uniform, efficient GPU operation.

### B. Robust Outlier Removal

Outliers are common in a SfM system and can adversely affect the accuracy of LM convergence. These outlier 3D points typically arise when a point is observed by only a small number of cameras, or when its reprojections lie outside the viewing frusta of all cameras. However, excluding outliers in a global SfM is inherently difficult because point visibility and reprojection behavior change as camera poses and 3D structure are updated during optimization: a point classified as an outlier early may become valid later and vice versa.

Prior works typically remove such outliers only once during preprocessing or rely on fixed robust loss functions during optimization, due to limitations of common optimization frameworks that do not natively support iterative, geometry-aware pruning inside the LM loop. This one-shot visibility

check risks discarding useful constraints or retaining harmful ones, because the nonlinearity of reprojection geometry tightly couples point validity with the current estimate: small updates to intrinsics or poses can shift reprojections across frustum boundaries or dramatically alter the inlier-outlier status of marginal points. A heuristic-based cost function cannot fully resolve the outlier problem either, because it merely down-weights large residuals without considering geometric visibility or consistency across multiple views. As a result, the optimizer may preserve geometrically invalid points that continue to bias the solution.

A further complication arises when a point temporarily loses all valid observations. One might consider simply zeroing out the residuals and gradients associated with such points, but this creates an ill-conditioned optimization problem as the corresponding columns of the Jacobian matrix become identically zero, producing rank deficiency in the normal equations and leading to singular or near-singular linear systems. In practice, this destabilizes LM updates, amplifies numerical noise, and can completely break convergence. These factors motivate our outlier rejection that is performed jointly with the evolving optimization state.

Our method integrates outlier detection directly into the optimization through a novel *dynamic parameter extraction* mechanism that maintains numerical stability while adapting to evolving geometry. The key innovation here lies in how we restructure the optimization problem at each iteration to include only geometrically valid observations and their associated parameters. Specifically,

1) We construct the complete set of potential observations from all registered tracks and cameras at the beginning of each LM iteration. We then perform a geometry validity check; each 3D point is projected into its observing cameras’ coordinate frames, and observations where the projected depth is non-positive or out-of-frustum are marked as invalid. This yields a filtered observation set with corresponding camera and point indices:

$$\mathcal{O}_{\text{valid}} = \{(i_c, i_p) \mid z_{i_c, i_p} > 0.1\}, \quad (10)$$

where  $i_c$  and  $i_p$  denote the array indices of the full camera and point parameters, respectively. The critical challenge is that after filtering, many cameras and points may have no remaining valid observations, yet their parameters still occupy entries in the full parameter vector  $\mathbf{x} \in \mathbb{R}^{n_{\text{total}}}$ . Including these inactive parameters in the optimization would yield a Jacobian  $\mathbf{J} \in \mathbb{R}^{m \times n_{\text{total}}}$  with all-zero columns, which in turn makes  $\mathbf{J}^T \mathbf{J}$  singular and the LM update unsolvable.

2) Then we identify the unique set of cameras and points that participate in at least one valid observation,

$$\mathcal{C}_{\text{active}} = \{\text{unique}(i_c \mid (i_c, i_p) \in \mathcal{O}_{\text{valid}})\} \quad (11)$$

$$\mathcal{P}_{\text{active}} = \{\text{unique}(i_p \mid (i_c, i_p) \in \mathcal{O}_{\text{valid}})\}, \quad (12)$$

where the unique set operation is achieved in a highly efficient SIMD manner, *e.g.* by `torch.unique`. We then extract

TABLE I  
COMPARISON ON THE MIPNERF360 DATASET [44] USING THE NVS METRIC.

	PSNR $\uparrow$				SSIM $\uparrow$				LPIPS $\downarrow$			
	COLMAP	GLOMAP	VGGsFM	Ours	COLMAP	GLOMAP	VGGsFM	Ours	COLMAP	GLOMAP	VGGsFM	Ours
bicycle	20.75	25.97	25.81	25.73	0.576	0.791	0.783	0.780	0.384	0.156	0.162	0.162
bonsai	19.86	32.96	32.56	32.06	0.619	0.957	0.953	0.947	0.490	0.054	0.056	0.061
counter	29.10	29.26	29.29	29.23	0.913	0.916	0.916	0.915	0.092	0.091	0.092	0.092
garden	27.91	27.80	27.74	27.66	0.878	0.876	0.875	0.869	0.072	0.073	0.073	0.077
kitchen	32.09	16.11	15.96	27.79	0.947	0.388	0.390	0.845	0.046	0.880	0.878	0.117
room	31.54	31.96	31.91	31.04	0.936	0.937	0.936	0.925	0.085	0.083	0.085	0.102
stump	27.21	26.61	26.51	25.53	0.797	0.760	0.758	0.711	0.143	0.164	0.168	0.184
Average	26.92	● 27.24	27.11	● 28.43	0.809	● 0.804	0.802	● 0.856	● 0.187	0.214	0.216	● 0.113

All experiments use `images_4` from the dataset, which is  $4\times$  downsampled from the original 4K raw data, resulting in around 1K resolution.

only these active parameters into a compact representation:

$$\hat{\mathbf{c}} = \mathbf{c}[\mathcal{C}_{\text{active}}] \in \mathbb{R}^{|\mathcal{C}_{\text{active}}| \times d_c} \quad (13)$$

$$\hat{\mathbf{p}} = \mathbf{p}[\mathcal{P}_{\text{active}}] \in \mathbb{R}^{|\mathcal{P}_{\text{active}}| \times 3} \quad (14)$$

where  $\mathbf{c}$  and  $\mathbf{p}$  are the full camera and point parameter arrays, and  $d_c$  is the camera parameter dimension. Crucially, we also construct a remapping from the original observation indices to the compacted index space:

$$\tilde{i}_c = \text{rank}(i_c \text{ in } \mathcal{C}_{\text{active}}), \quad \tilde{i}_p = \text{rank}(i_p \text{ in } \mathcal{P}_{\text{active}}) \quad (15)$$

This remapping ensures that the residual computation in the forward pass correctly indexes into  $\hat{\mathbf{c}}$  and  $\hat{\mathbf{p}}$ .

The resulting optimization problem operates entirely in the compacted space with  $\hat{n} = |\mathcal{C}_{\text{active}}| \cdot d_c + |\mathcal{P}_{\text{active}}| \cdot 3$  parameters and  $m = |\mathcal{O}_{\text{valid}}| \cdot 2$  residuals (for 2D reprojection). Critically, every parameter in  $\hat{\mathbf{x}} = [\hat{\mathbf{c}}; \hat{\mathbf{p}}]$  appears in at least one residual by construction, guaranteeing that the Jacobian  $\hat{\mathbf{J}} \in \mathbb{R}^{m \times \hat{n}}$  has no all-zero columns. The normal equations  $\hat{\mathbf{J}}^\top \hat{\mathbf{J}} \delta \hat{\mathbf{x}} = -\hat{\mathbf{J}}^\top \mathbf{r}$  are thus full-rank (up to gauge freedom), and the LM step remains well-conditioned even when a large fraction of points are temporarily invalid.

3) After computing the update  $\delta \hat{\mathbf{x}}$  via preconditioned conjugate gradient, we scatter the updates back to the original parameter arrays using the inverse of the index mappings. Parameters not in  $\mathcal{C}_{\text{active}}$  or  $\mathcal{P}_{\text{active}}$  remain unchanged for that iteration. At the next iteration, visibility is re-evaluated with the updated poses and structure, and the compaction process repeats, potentially activating different subsets of parameters as geometry evolves. This *dynamic parameter extraction* mechanism enables our optimizer to seamlessly handle points that transition between valid and invalid states throughout the optimization. Unlike static outlier rejection schemes that commit to a fixed residual structure, or robust kernels that merely down-weight residuals without addressing rank deficiency, our approach fundamentally adapts the problem dimensionality to match the current geometric configuration. This ensures numerical stability across all optimization stages while naturally excluding degenerate observations.

## V. EXPERIMENT

We evaluate InstantSfM against state-of-the-art SfM systems on multiple datasets, assessing both reconstruction efficiency and efficiency. We conduct comparisons of VGGsFM [33], COLMAP [10], GLOMAP [11], and our InstantSfM

on a platform with an Intel Xeon Platinum 8480C and an NVIDIA H200 GPU (140.4 GB), to avoid out-of-memory issues of VGGsFM [33] when handling large-scale scenes. For a fair comparison with COLMAP and GLOMAP, we use RootSIFT for feature extraction and keep the same feature matching results for the three methods.

**Evaluation Criteria.** We evaluate on (a) rendering quality with 3DGS [14], and (b) 3D map reconstruction accuracy. We report novel view synthesis (NVS) metrics (e.g., PSNR, SSIM, and LPIPS) by training 3D Gaussian Splatting [9] using the estimated camera poses and 3D map reconstruction points as an initialization. We also measure the Chamfer distance on datasets with reliable ground-truth point cloud scan to demonstrate 3D map reconstruction accuracy.

### A. Performance on Various Datasets

**MipNeRF360** [44] is a 360-degree object-centric dataset of 7 scenes. We use  $4\times$  downsampled images following [33] and report NVS metrics in Table I, in which our system achieves the best overall performance among all metrics.

**DTU** [45] is an object-centric dataset of 119 scans with ground-truth geometry from structured light scanning. We evaluate under the medium lighting condition (condition 5) and report NVS metrics in Table II.

**ScanNet** [46] is a large-scale RGB-D indoor scan dataset. On ScanNet (Table III), both COLMAP and GLOMAP fail on most scenes: GLOMAP due to Ceres solver divergence in its ViewGraphCalibration step, and COLMAP due to incomplete reconstructions, while InstantSfM succeeds on all scenes and improves further with depth priors.

**ScanNet++** [47] is a large-scale high-fidelity RGB-D indoor scan dataset. On ScanNet++ (Table IV), InstantSfM consistently outperforms GLOMAP, achieving an average Chamfer distance of 2.61 compared to GLOMAP’s 3.80.

### B. Running Time Analysis

#### Runtime Comparisons with COLMAP and GLOMAP.

We compare InstantSfM’s running time with COLMAP and GLOMAP on scenes ranging from 100 to 5,000 images, as shown in Fig. 3. Specifically, scenes with 100 images are selected from the MipNeRF360 [44] dataset through downsampling, while larger scenes (300-5,000 images) are obtained by downsampling from the 1DSfM [48] dataset. This selection strategy is adopted because the 1DSfM dataset,

TABLE II  
QUANTITATIVE EVALUATION FOR SfM METHODS ON DTU DATASET.

	PSNR $\uparrow$			SSIM $\uparrow$			LPIPS $\downarrow$		
	COLMAP	GLOMAP	Ours	COLMAP	GLOMAP	Ours	COLMAP	GLOMAP	Ours
scan002	21.83	20.77	22.80	0.872	0.862	0.868	0.094	0.166	0.096
scan016	24.94	24.18	24.04	0.892	0.891	0.899	0.075	0.237	0.067
scan033	23.45	7.192	22.11	0.911	0.356	0.907	0.075	0.860	0.081
scan047	22.91	7.470	24.49	0.909	0.409	0.913	0.104	0.510	0.091
scan062	23.71	25.85	25.56	0.907	0.919	0.909	0.076	0.248	0.070
scan077	23.40	13.41	21.50	0.928	0.715	0.907	0.100	0.882	0.140
scan095	24.00	17.49	20.80	0.867	0.659	0.769	0.153	0.693	0.240
scan109	30.13	28.32	28.98	0.911	0.902	0.901	0.151	0.166	0.158
scan123	30.64	17.16	30.83	0.910	0.580	0.913	0.212	0.228	0.211
Average	● 25.00	17.98	● 24.57	● 0.901	0.699	● 0.887	● 0.116	0.443	● 0.128

TABLE III  
CHAMFER DISTANCE ( $\downarrow$ ) COMPARISON ON SCANNET.

	COLMAP	GLOMAP	Ours (w/o depth)	Ours (w/ depth)
0001.00	3.358	FAILED	0.557	0.987
0001.01	FAILED	FAILED	0.768	0.646
0002.00	FAILED	FAILED	0.244	0.208
0002.01	FAILED	FAILED	0.205	0.195
0003.00	0.4139	FAILED	2.353	1.098
0003.01	0.2478	FAILED	1.211	1.047
0003.02	0.2337	FAILED	0.556	0.428
Average	FAILED	FAILED	0.842	0.658

FAILED: optimization failure with no output. Ours (w/o depth): InstantSfM without depth prior. Ours (w/ depth): InstantSfM with depth prior.

TABLE IV  
CHAMFER DISTANCE ( $\downarrow$ ) COMPARISON ON SCANNET++.

	COLMAP	GLOMAP	Ours (w/o depth)
0f69ae...	5.75	1.67	0.92
ff1765...	2.38	3.85	2.71
8c3169...	5.90	3.36	1.05
00777c...	5.24	5.38	5.22
00a231...	2.90	4.74	3.15
Average	4.43	3.80	2.61

with its large-scale scenes, would be difficult to effectively match when downsampled to only 100 images.

**Runtime Comparisons with GPU-accelerated Methods.** We report comparisons with COLMAP and GLOMAP equipped with GPU-accelerated Ceres Solver. At the time of our experiments, neither COLMAP nor GLOMAP provided GPU acceleration for the evaluated pipeline. More recent versions have introduced GPU-enabled installations of Ceres Solver, which are expected to further improve computational efficiency. Despite demonstrable efficiency improvements with GPU acceleration, COLMAP and GLOMAP still lag behind our method, as shown in Table V.

## VI. CONCLUSION

We presented InstantSfM, a GPU-native and PyTorch-compatible global SfM system. By combining a depth-constrained Jacobian structure for metric scale recovery with dynamic parameter extraction for robust outlier handling, InstantSfM enables a complete and numerically stable global

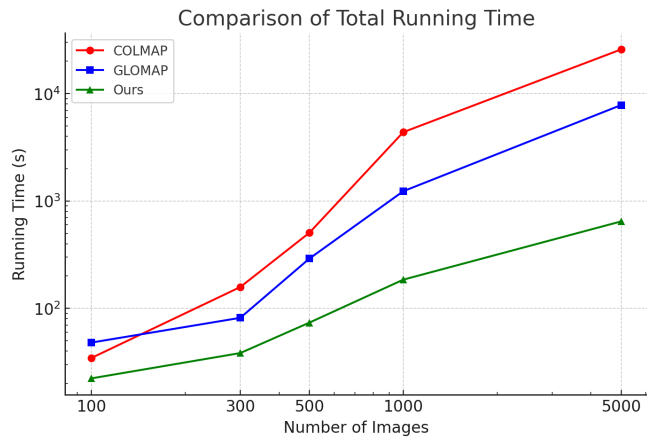


Fig. 3. Comparisons of total SfM runtime of COLMAP, GLOMAP and InstantSfM on different numbers of images. Runtime is in **log space**.

TABLE V  
GPU RUNTIME(S) COMPARISON WITH COLMAP/GLOMAP

Dataset	COLMAP	GLOMAP	Ours
Alamo	12855.4	1599.5	<b>597.0</b>
Madrid_Metropolis	1661.5	440.7	<b>222.9</b>
Union_Square	4696.7	966.4	<b>571.3</b>

SfM within a unified GPU optimization framework. Experiments show InstantSfM achieves competitive reconstruction quality while delivering up to  $\sim 40\times$  speedup over COLMAP and up to  $12\times$  over GLOMAP on large-scale scenes.

The current system is primarily designed for single-node execution, which may limit scalability to extremely large problems. Future work includes extending InstantSfM to distributed settings and improving robustness under more challenging imaging conditions.

## REFERENCES

- [1] S. Agarwal, Y. Furukawa, N. Snavely, I. Simon, B. Curless, S. M. Seitz, and R. Szeliski, "Building rome in a day," *Communications of the ACM*, vol. 54, no. 10, pp. 105–112, 2011.
- [2] J.-M. Frahm, P. Fite-Georgel, D. Gallup, T. Johnson, R. Raguram, C. Wu, Y.-H. Jen, E. Dunn, B. Clipp, S. Lazebnik *et al.*, "Building rome on a cloudless day," in *Computer Vision—ECCV 2010: 11th European Conference on Computer Vision, Heraklion, Crete, Greece, September 5–11, 2010, Proceedings, Part IV 11*. Springer, 2010, pp. 368–381.
- [3] L. MacDonald, *Digital heritage*. Routledge, 2006.

- [4] Z. Chen, J. Yang, J. Huang, R. de Lutio, J. M. Esturo, B. Ivanovic, O. Litany, Z. Gojcic, S. Fidler, M. Pavone, L. Song, and Y. Wang, "Omni-nire: Omni urban scene reconstruction," in *The Thirteenth International Conference on Learning Representations*, 2025.
- [5] Z. Li, R. Tucker, F. Cole, Q. Wang, L. Jin, V. Ye, A. Kanazawa, A. Holynski, and N. Snavely, "Megsam: Accurate, fast, and robust structure and motion from casual dynamic videos," *arXiv preprint arXiv:2412.04463*, 2024.
- [6] H. Lou, Y. Liu, Y. Pan, Y. Geng, J. Chen, W. Ma, C. Li, L. Wang, H. Feng, L. Shi, L. Luo, and Y. Shi, "Robo-GS: A physics consistent spatial-temporal model for robotic arm with hybrid representation," in *IEEE International Conference on Robotics and Automation (ICRA)*, 2025. [Online]. Available: <https://arxiv.org/abs/2408.14873>
- [7] R. I. Hartley, R. Gupta, and T. Chang, "Stereo from uncalibrated cameras." in *CVPR*, vol. 92, 1992, pp. 761–764.
- [8] B. Mildenhall, P. P. Srinivasan, M. Tancik, J. T. Barron, R. Ramamoorthi, and R. Ng, "Nerf: Representing scenes as neural radiance fields for view synthesis," *Communications of the ACM*, vol. 65, no. 1, pp. 99–106, 2021.
- [9] B. Kerbl, G. Kopanas, T. Leimkühler, and G. Drettakis, "3d gaussian splatting for real-time radiance field rendering." *ACM Trans. Graph.*, vol. 42, no. 4, pp. 139–1, 2023.
- [10] J. L. Schönberger and J.-M. Frahm, "Structure-from-motion revisited," in *Conference on Computer Vision and Pattern Recognition (CVPR)*, 2016.
- [11] L. Pan, D. Baráth, M. Pollefeys, and J. L. Schönberger, "Global structure-from-motion revisited," in *European Conference on Computer Vision*. Springer, 2024, pp. 58–77.
- [12] S. Agarwal, K. Mierle, and The Ceres Solver Team, "Ceres Solver," Oct. 2023. [Online]. Available: <https://github.com/ceres-solver/ceres-solver>
- [13] J. Wang, M. Chen, N. Karaev, A. Vedaldi, C. Rupprecht, and D. Novotny, "Vggt: Visual geometry grounded transformer," in *Proceedings of the Computer Vision and Pattern Recognition Conference*, 2025, pp. 5294–5306.
- [14] V. Ye, R. Li, J. Kerr, M. Turkulainen, B. Yi, Z. Pan, O. Seiskari, J. Ye, J. Hu, M. Tancik, and A. Kanazawa, "gsplat: An open-source library for gaussian splatting," *Journal of Machine Learning Research*, vol. 26, no. 34, pp. 1–17, 2025.
- [15] C. Wang, K. Ji, J. Geng, Z. Ren, T. Fu, F. Yang, Y. Guo, H. He, X. Chen, Z. Zhan, Q. Du, S. Su, B. Li, Y. Qiu, Y. Du, Q. Li, Y. Yang, X. Lin, and Z. Zhao, "Imperative learning: A self-supervised neuro-symbolic learning framework for robot autonomy," *International Journal of Robotics Research (IJRR)*, 2025. [Online]. Available: <https://arxiv.org/abs/2406.16087>
- [16] Z. Zhan, D. Gao, Y.-J. Lin, Y. Xia, and C. Wang, "iMatching: Imperative correspondence learning," in *European Conference on Computer Vision (ECCV)*, 2024. [Online]. Available: <https://arxiv.org/pdf/2312.02141.pdf>
- [17] Z. Zhan, H. Xu, Z. Fang, X. Wei, Y. Hu, and C. Wang, "Bundle adjustment in the eager mode," *arXiv preprint arXiv:2409.12190*, 2024.
- [18] L. Pineda, T. Fan, M. Monge, S. Venkataraman, P. Sodhi, R. T. Chen, J. Ortiz, D. DeTone, A. Wang, S. Anderson, J. Dong, B. Amos, and M. Mukadam, "Theseus: A Library for Differentiable Nonlinear Optimization," *Advances in Neural Information Processing Systems*, 2022.
- [19] J. Huang, S. Huang, and M. Sun, "DeepIm: Large-scale nonlinear least squares on deep learning frameworks using stochastic domain decomposition," in *Proceedings of the IEEE/CVF Conference on Computer Vision and Pattern Recognition*, 2021, pp. 10 308–10 317.
- [20] T. Fan, J. Ortiz, M. Hsiao, M. Monge, J. Dong, T. Murphey, and M. Mukadam, "Decentralization and acceleration enables large-scale bundle adjustment," in *Robotics: Science and Systems*, 2023.
- [21] D. G. Lowe, "Distinctive image features from scale-invariant keypoints," *International journal of computer vision*, vol. 60, pp. 91–110, 2004.
- [22] D. DeTone, T. Malisiewicz, and A. Rabinovich, "Superpoint: Self-supervised interest point detection and description," in *Proceedings of the IEEE conference on computer vision and pattern recognition workshops*, 2018, pp. 224–236.
- [23] J. Sun, Z. Shen, Y. Wang, H. Bao, and X. Zhou, "Loftr: Detector-free local feature matching with transformers," in *Proceedings of the IEEE/CVF conference on computer vision and pattern recognition*, 2021, pp. 8922–8931.
- [24] Y. Wang, X. He, S. Peng, D. Tan, and X. Zhou, "Efficient loftr: Semi-dense local feature matching with sparse-like speed," in *Proceedings of the IEEE/CVF Conference on Computer Vision and Pattern Recognition*, 2024, pp. 21 666–21 675.
- [25] P.-E. Sarlin, D. DeTone, T. Malisiewicz, and A. Rabinovich, "Superglue: Learning feature matching with graph neural networks," in *Proceedings of the IEEE/CVF conference on computer vision and pattern recognition*, 2020, pp. 4938–4947.
- [26] M. A. Fischler and R. C. Bolles, "Random sample consensus: a paradigm for model fitting with applications to image analysis and automated cartography," *Communications of the ACM*, vol. 24, no. 6, pp. 381–395, 1981.
- [27] R. I. Hartley and P. Sturm, "Triangulation," *Computer vision and image understanding*, vol. 68, no. 2, pp. 146–157, 1997.
- [28] N. Snavely, "Bundler: Structure from motion (sfm) for unordered image collections," 2010. [Online]. Available: <http://phototour.cs.washington.edu/bundler/>
- [29] P.-E. Sarlin, M. Dusmanu, J. L. Schönberger, P. Speciale, L. Gruber, V. Larsson, O. Miksik, and M. Pollefeys, "LaMAR: Benchmarking Localization and Mapping for Augmented Reality," in *ECCV*, 2022.
- [30] N. Jiang, Z. Cui, and P. Tan, "A global linear method for camera pose registration," in *Proceedings of the IEEE international conference on computer vision*, 2013, pp. 481–488.
- [31] P. Moulon, P. Monasse, and R. Marlet, "Global fusion of relative motions for robust, accurate and scalable structure from motion," in *Proceedings of the IEEE international conference on computer vision*, 2013, pp. 3248–3255.
- [32] Rother, "Linear multiview reconstruction of points, lines, planes and cameras using a reference plane," in *Proceedings Ninth IEEE International Conference on Computer Vision*. IEEE, 2003, pp. 1210–1217.
- [33] J. Wang, N. Karaev, C. Rupprecht, and D. Novotny, "Vggsfm: Visual geometry grounded deep structure from motion," in *Proceedings of the IEEE/CVF conference on computer vision and pattern recognition*, 2024, pp. 21 686–21 697.
- [34] Q. Wang, Y. Zhang, A. Holynski, A. A. Efros, and A. Kanazawa, "Continuous 3d perception model with persistent state," *arXiv preprint arXiv:2501.12387*, 2025.
- [35] S. Wang, V. Leroy, Y. Cabon, B. Chidlovskii, and J. Revaud, "Dust3r: Geometric 3d vision made easy," in *Proceedings of the IEEE/CVF Conference on Computer Vision and Pattern Recognition*, 2024, pp. 20 697–20 709.
- [36] A. Ranganathan, "The levenberg-marquardt algorithm," *Tutorial on LM algorithm*, vol. 11, no. 1, pp. 101–110, 2004.
- [37] F. Dellaert and G. Contributors, "borglab/gtsam," 2022.
- [38] H. Han and H. Yang, "Building rome with convex optimization," *arXiv preprint arXiv:2502.04640*, 2025.
- [39] R. Hartley, J. Trunpf, Y. Dai, and H. Li, "Rotation averaging," *International journal of computer vision*, vol. 103, pp. 267–305, 2013.
- [40] V. M. Govindu, "Combining two-view constraints for motion estimation," in *Proceedings of the 2001 IEEE computer society conference on computer vision and pattern recognition*. CVPR 2001, vol. 2. IEEE, 2001, pp. II–II.
- [41] P. J. Huber, "Robust estimation of a location parameter," in *Breakthroughs in statistics: Methodology and distribution*. Springer, 1992, pp. 492–518.
- [42] L. Xuan, C. Nie, Y. Xu, Z. Liu, Y. Miao, and H. Wang, "Mrasfm: Multi-camera reconstruction and aggregation through structure-from-motion in driving scenes," 2025. [Online]. Available: <https://arxiv.org/abs/2510.15467>
- [43] J. Huang, Q. Zhou, H. Rabeti, A. Korovko, H. Ling, X. Ren, T. Shen, J. Gao, D. Slepichev, C.-H. Lin, J. Ren, K. Xie, J. Biswas, L. Leal-Taixe, and S. Fidler, "Vipe: Video pose engine for 3d geometric perception," in *NVIDIA Research Whitepapers arXiv:2508.10934*, 2025.
- [44] J. T. Barron, B. Mildenhall, D. Verbin, P. P. Srinivasan, and P. Hedman, "Mip-nerf 360: Unbounded anti-aliased neural radiance fields," in *Proceedings of the IEEE/CVF conference on computer vision and pattern recognition*, 2022, pp. 5470–5479.
- [45] R. Jensen, A. Dahl, G. Vogiatzis, E. Tola, and H. Aanaes, "Large scale multi-view stereopsis evaluation," in *Proceedings of the IEEE Conference on Computer Vision and Pattern Recognition (CVPR)*, 2014.
- [46] A. Dai, A. X. Chang, M. Savva, M. Halber, T. Funkhouser, and M. Nießner, "ScanNet: Richly-annotated 3d reconstructions of indoor scenes," in *Proc. Computer Vision and Pattern Recognition (CVPR)*, IEEE, 2017.
- [47] C. Yeshwanth, Y.-C. Liu, M. Nießner, and A. Dai, "ScanNet++: A high-fidelity dataset of 3d indoor scenes," in *Proceedings of the International Conference on Computer Vision (ICCV)*, 2023.

- [48] K. Wilson and N. Snavely, "Robust global translations with 1dsfm," in *European conference on computer vision*. Springer, 2014, pp. 61–75.